Available online at www.sciencedirect.com
ScienceDirect
Trans. Nonferrous Met. Soc. China 34(2024) 1588−1605
Transactions of Nonferrous Metals Society of China
www.tnmsc.cn

Microstructure and grain evolution mechanisms of copper/steel explosive welding interface

Ming YANG[1], Bing-yuan ZHANG[2], Hong-hao MA[2,3], Jin-xiang WANG[1], Jia-yi XIONG[1]

1. National Key Laboratory of Transient Physics, Nanjing University of Science and Technology, Nanjing 210094, China;
2. CAS Key Laboratory of Mechanical Behavior and Design of Materials, University of Science and Technology of China, Hefei 230026, China;
3. State Key Laboratory of Fire Science, University of Science and Technology of China, Hefei 230026, China

Received 31 October 2022; accepted 13 June 2023

Abstract: By integrating smoothed particles hydrodynamics (SPH) simulation, advanced characterization, and theoretical analysis, the interfacial transient behaviors of copper/steel composite during explosive welding were deeply studied, and the evolution mechanisms of microstructures were specifically explained. According to simulated data, the entire evolution of wave was reconstructed, and the formation mechanisms of various interface features were revealed. The multi-scale EBSD analyses showed that the grain structures were diverse in the regions adjacent to the interfaces. The evolution mechanisms of these grains were mainly governed by three processes of plastic flow, dynamic recrystallization, and solidified nucleation. Finally, the correlations between the grain structures and mechanical properties were established by nanoindentation tests.

Key words: explosive welding; copper/steel composite; wave-forming mechanism; grain structure; nanoindentation

1 Introduction

The high velocity impact welding (HVIW) technologies are becoming increasingly attractive for producing structural composite materials, as they offer good competitive advantages like higher bonding strength and less microstructure degradation when compared to conventional fusion-based welding processes [1,2]. Explosive welding (EW) is the most commonly utilized HVIW technology, in which the flyer plate is accelerated towards the stationary base plate by explosion energy, leading to a high-speed impact and subsequent formation of a metallurgical bond between the two welded plates [3,4]. As proved by the simulation works [5,6], the EW process is completed in microseconds, while the joint interface is subjected to an extreme condition of large strain rate of ~10^7 s^{-1}, high temperature of ~2000 K and high pressure up to 1−10 GPa. It is foreseeable that the harsh thermomechanical condition will induce a series of unusual materials responses, viz., strong plastic flow and material spalling [7], localized melt and quench [8,9], crystal structure evolution and phase transformation [10,11], intense mechanical mixing and even chemical reaction [12,13]. However, since the in-situ observations are extremely difficult, many fundamental aspects about the EW interface formation remain an open topic of discussion.

Waves are undoubtedly the most remarkable

Corresponding author: Bing-yuan ZHANG: Tel: +86-18555150112, E-mail: zhangbingyuan@mail.ustc.edu.cn;
Hong-hao MA: Tel: +86-17755131576, E-mail: hhma@ustc.edu.cn
DOI: 10.1016/S1003-6326(24)66493-9

characteristics of the EW interfaces, and are perceived to improve bonding strength by mechanical interlocking. Several mechanisms, referring to indentation mechanism [14,15], flow instability mechanism [16,17], vortex shedding mechanism [18], and stress wave mechanism [19], have been put forth to explain the wave formation. Although these mechanisms are supported by some experimental data, they have not been proven to have universal applications yet. Meanwhile, they are not mutually exclusive either and several of them are even related with each other depending upon certain welding conditions. In addition, only a little attention was devoted to investigating the shape evolutions of the waves and the associated mechanisms. For example, the detailed origins of branch structure at the crest and the asymmetry of a specific wave are not well understood, and fundamental formation mechanisms of melt pockets that accompany the material intermixing and fragments remain unclear. We attribute the lack of in-depth understanding on the operative mechanisms, to the difficulties in observing the microstructure evolution in situ and the challenges to predict the large deformed wave interface via conventional finite-element-based methods. Recently, due to the rapid development of meshless numerical methods, smoothed particles hydrodynamics (SPH) was proved to be a suitable method to deal with the large deformation problem induced by high speed collision, by which the most important interface features (including formation of jet, wavy boundary, and vortex) and thermo-mechanical conditions (such as temperature and pressure) during the EW process could be accurately reproduced [20−23]. Thus, such models may help to explain post-weld experimental observations, and provide in-depth understanding of the interface evolution.

The impact-induced extreme thermo-mechanical conditions not only produce complex and heterogeneous interfaces, but also lead to profound grain evolutions. In view of the importance of grain structures in determining the mechanical properties of composites, numerous studies have been performed to reveal the grain features at the EW interface, and the main findings can be summarized as: flattened elongated grains [1], highly curve grains [24,25], equiaxed grains [26,27], columnar grains [28], nanoscale grains [29], and amorphous structure [30,31]. These grains are distributed at different positions of the EW interface, and contain significant information that may be used for understanding the interface evolution. Although abundant works have been dedicated to the newly formed grains, a comprehensive correlation between the grain characteristics and distribution regions is yet to be established. Moreover, the formation mechanisms of various grains, which depend on the material compositions and thermodynamics history, remain insufficient exploration and require more detailed consideration. The absence of the sophisticated understanding is mainly due to the lack of in-depth study of characterizing the diversity of grain structure. Such studies need to resolve intractable contradictions between high resolution requirements for the ultrafine nanoscale grains and large areas demands for the elongated large grains.

This work is intended to investigate the interfacial transient behaviors during the EW process, and specifically explain the mechanisms of wave shape evolution, melt pocket formation, and grain structure. Copper/steel (Cu/Fe) clad was used as a model system, due to its universality in both industry and academia. The general morphologies at the interface were studied by scanning electron microscope (SEM) cooperated with energy dispersive spectrometer (EDS). A multi-scale electron backscattered diffraction (EBSD) analysis was performed to fully reveal the grain features, and the corresponding nano-mechanical properties were investigated by nanoindentation tests. To explain the observed phenomena, the microstructure evolutions and thermomechanical effects at the Cu/Fe interface were systematically investigated by SPH simulation. This comprehensive study enables to improve the understanding of the HVIW process, and offers the guidance for property optimization and industrial application of the composite.

2 Experimental

2.1 Experimental procedure

Figure 1 presents an installation diagram of the EW experiment. The flyer plate and base plate were made by commercially pure Cu and reduced activation ferritic-martensitic (RAFM) steel, with corresponding dimensions of 150 mm × 80 mm × 2 mm and 200 mm × 120 mm × 10 mm, respectively.

The chemical components of the two plates are listed in Tables 1 and 2, respectively, and the air gap between the two plates was 8 mm. Prior to explosion, their surfaces to be welded were processed by mechanical sanding and acetone cleaning. Emulsion explosives, with thickness of 12 mm, detonation velocity of ~2700 m/s and density of 0.85 g/cm^3, were chosen as the explosive materials, which were placed on the flyer plate. These initial settings resulted in transient collision angle of 8.1° and impact velocity of 382 m/s, and the corresponding computational equations are described below [25,32]:

$$v_p=\sqrt{2E}\left[\frac{1+A^3}{3(1+A)}+\frac{M}{C}\right]^{-1/2}\cdot\left[1-\left(\frac{T_e}{T_e+(1+A)s}\right)^{\gamma-1}\right]^{1/2} \quad (1)$$

where

$$A=1+2\frac{M}{C} \quad (2)$$

$$E=\frac{1}{\gamma^2-1}\left(\frac{\gamma}{\gamma-1}\right)^{\gamma}v_d^2 \quad (3)$$

$$v_p=2v_c\sin(\beta/2) \quad (4)$$

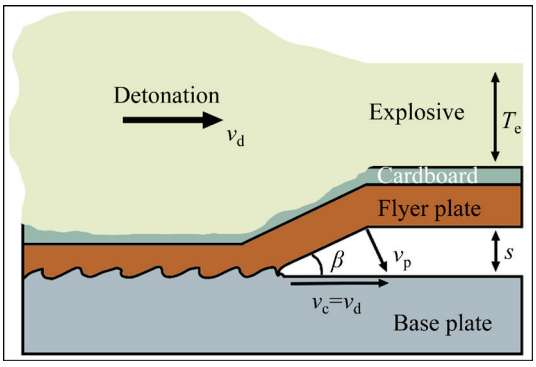

Fig. 1 Schematic diagram of EW process

Table 1 Chemical composition of commercially pure Cu (wt.%)

Cu	Fe	Ni	Bi	Sb	Zn	As	O
Bal. (≥99.95)	0.005	0.002	0.001	0.002	0.005	0.002	0.002

Table 2 Chemical composition of RAFM steel (wt.%)

Fe	Cr	W	V	Ta	Mn	C	N
Bal.	8.93	1.43	0.20	0.12	0.68	0.09	0.04

where v_p is the impact velocity, C and M are the mass per unit of the explosive and the flyer plate, respectively, v_d is the detonation velocity, s is the displacement of the flyer plate, T_e is the initial thickness of explosives, v_c is the collision point speed equal to the detonation velocity in this work, β is the collision angle, and γ is the polytropic exponent of detonation products.

For the microstructure analysis, a small rectangular specimen was extracted from the middle position of the weldment, which was then polished by standard metallographic steps. Based on it, a SEM (GeminiSEM 500 equipped EDS detectors) was used to reveal the microstructures and element distributions of the bonding interfaces. The EDS element analysis was carried out using a working distance of 8.5 mm and an accelerating voltage of 20 kV. For EBSD test, to remove the residual stress from previous mechanical polishing, the specimen was further polished with argon ion. The EBSD scanning was carried out using an accelerating voltage of 20 kV and a working distance of 13 mm, and the minimum step size was set to be only 40 nm to display the possible formed ultrafine grains. Finally, the nanoindentation tests were performed with a consistent loading speed of 500 μN/s and a peak load of 15 mN.

2.2 Numerical simulation

As displayed in Fig. 2, a two-dimensional model was developed in Autodyn code for simulating the EW process. Compared to the actual situation, the model ignored the driving process of explosive to flyer plate and just involved an inclined impact configuration composed of two welded plates. The initial impact conditions

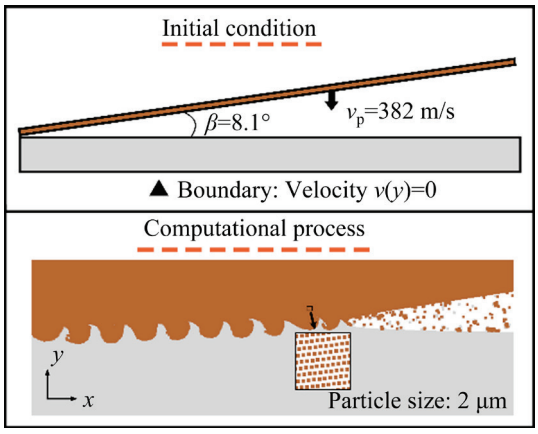

Fig. 2 Basic setup of simulation model

consisted of impact velocity and angle, which were obtained by theoretical calculations. To save the computing resources, the lengths of the two plates were set to be only 20 mm (the thicknesses of the two plates were consistent with the experiment). The SPH processor was selected for its meshless nature, which was very suitable for solving problems associated with large strains and enabled to precisely describe the material deformation of the weld interface. The detailed description of SPH method can be found in previous work [20,21,33], and the corresponding governing equations are given as follows:

$$\frac{\mathrm{d}\rho}{\mathrm{d}t}=-\rho\frac{\partial v^{\beta}}{\partial x^{\beta}} \tag{5}$$

$$\frac{\mathrm{d}v^{\alpha}}{\mathrm{d}t}=\frac{1}{\rho}\frac{\partial v^{\alpha\beta}}{\partial x^{\beta}} \tag{6}$$

$$\frac{\mathrm{d}e}{\mathrm{d}t}=-\frac{\boldsymbol{\sigma}_1^{\alpha\beta}}{\rho}\frac{\partial v^{\alpha}}{\partial x^{\beta}} \tag{7}$$

where

$$\boldsymbol{\sigma}_1=-P\boldsymbol{I}+\boldsymbol{S} \tag{8}$$

where ρ is density, t is time, e is internal energy, α and β are indicators of a tensor; v^{α} is velocity component, x^{β} is spatial coordinate, $\boldsymbol{\sigma}_1^{\alpha\beta}$ is total stress tensor, P is pressure, $\boldsymbol{I}$ is unit tensor, and $\boldsymbol{S}$ is stress partial tensor. Additionally, Johnson−Cook constitutive model and the Mie−Gruneisen equation of state (EOS) were employed to simulate the material dynamic behaviors, which correspond to Eqs. (9) and (10), respectively:

$$\sigma=\left(A+B\varepsilon_{\mathrm{eff}}^{n}\right)\left(1+C\ln\dot{\varepsilon}\right)\left(1-T_0^{m}\right) \tag{9}$$

where σ is flow stress, A, B, C, n, and m are the material parameters, $\varepsilon_{\mathrm{eff}}$ is effective plastic strain, $\dot{\varepsilon}(=\dot{\varepsilon}_{\mathrm{eff}}/\dot{\varepsilon}_0)$ is plastic strain rate, and $T_0(=(T-T_{\mathrm{room}})/(T_{\mathrm{melt}}-T_{\mathrm{room}}))$ is homologous temperature.

$$P=\frac{\rho_0 c_0\mu}{1-s_1\mu}\left(1-\frac{\Gamma_0\mu}{2}\right)+\Gamma_0\rho_0 e \tag{10}$$

where ρ_0 is initial density of materials, c_0 is the sonic speed, $\mu(=1-\rho/\rho_0)$ is the density change rate, Γ_0 is Gruneisen coefficient, and s_1 is the material constant. The necessary material parameters of constitutive and EOS equations are given in Table 3, which are obtained from the existing studies [34,35].

3 Results

3.1 Interface morphologies

Figure 3(a) shows a typical SEM image of the achieved Cu/Fe interface, revealing a regular wavy structure with a well-defined wavelength and amplitude of ~260 and ~100 μm, respectively. Figures 3(b) and (d) give the simulation results of material distributions. Clearly, the simulated waves show good agreements with the experimental ones regardless the shape and size, which suggests the validity of SPH method to further analyze the formation mechanism of the wave. The enlarged view given in Fig. 3(c) indicates that the individual wave is asymmetrical, where the left side of the wave presents an inward profile, while the right side is characterized by slight outward curve. Especially, there is a crab-claw-like structure at the upper left of the wave, as marked in Fig. 3(c). The inward profile together with the crab-claw-like outline constitutes a vortex boundary, in which a big melt pocket with a diameter of ~40 μm is formed, identified by different backscattered electron (BSE) contrasts (varying grey levels). In addition, the melted zones are also distributed along the interfaces, which have varying thicknesses from a few microns to approximately 30 μm. EDS line scanning reveals that the melted zone is built by mixture of participant metals, and the element changes are sharp across the interfaces between Cu (or Fe) matrix and the melted zone, as shown in Fig. 3(c). This observation implies that the formation of such a melted zone is governed by strong mechanical mixing of two welded materials [36]. In order to further understand the chemical compositions of the melted zones, EDS map scanning was carried out within three selected zones labeled in Fig. 3, and the corresponding results

Table 3 Constitutive and EOS parameters of Cu and Fe

Material	ρ_0/(g·cm^{-3})	c_0/(m·s^{-1})	s_1	Γ_0	γ/(J·kg·K^{-1})	T_{room}/K	T_{melt}/K	A/MPa	B/MPa	C	n	m
Cu	8.93	3940	1.489	1.99	385	298	1350	90	292	0.025	0.31	1.09
Fe	7.80	4569	1.49	1.67	452	298	1795	229	439	0.10	0.503	0.55

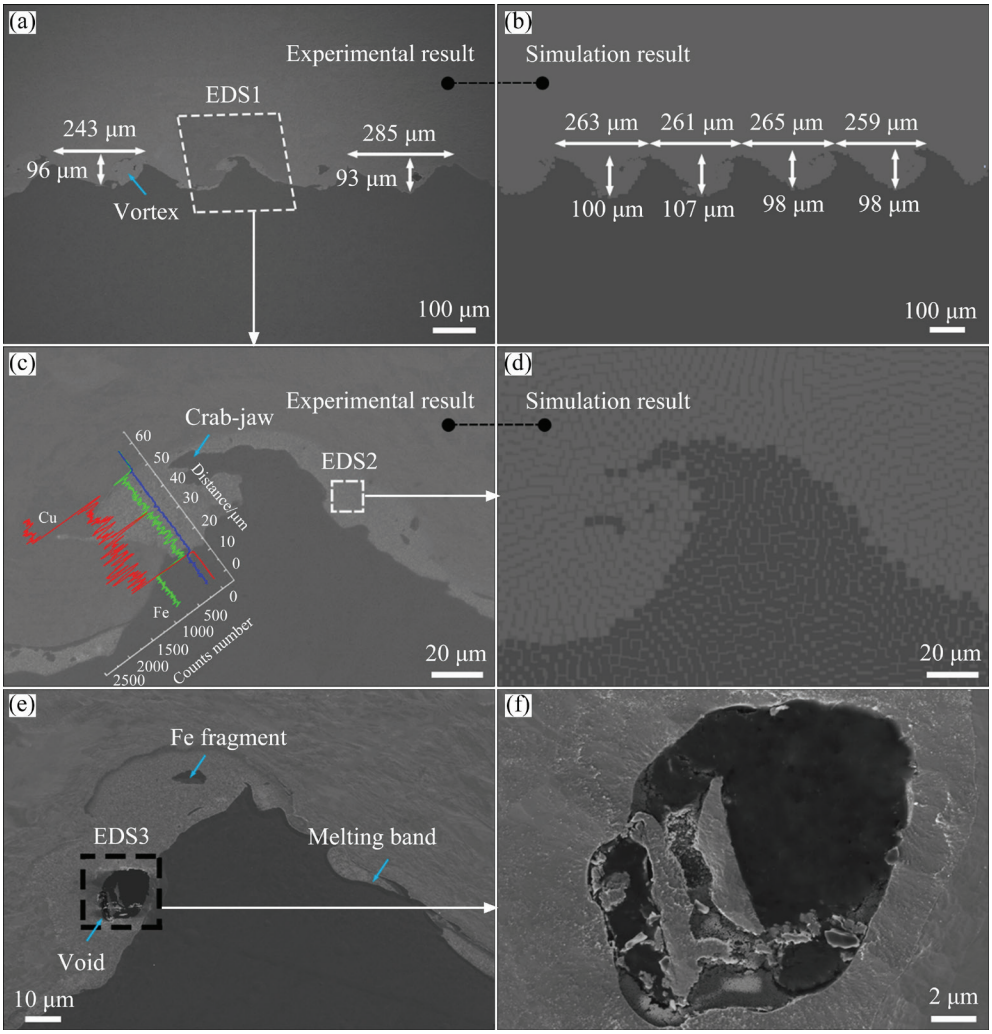

Fig. 3 Interface morphologies from SEM observation showing general layout of waves (a), individual wave (c, e), interior structure of void (f), and interface morphology obtained by SPH simulation (b, d)

are given in Fig. 4. The high-resolution maps (Figs. 4(d−f)) focusing on a localized area of the melted zone reveal an alternating colour contrast, indicating the inhomogeneity of the element distribution in this area. These maps also give an opportunity for quantitative analysis of chemical distributions, by which the phase of the melted zone is found to be $Cu_{0.75}Fe_{0.23}Cr_{0.02}$, indicating the average mass ratio of certain areas. In some situations, Fe fragments and voids can be found in the melted zone, as shown in Fig. 3(e). The enlarged view of this zone (Fig. 3(f)) reveals that the void is near spherical with a diameter of ~8 μm. The similar observation has also been made by LI et al [37], and they attributed its formation to physical kinematics rather than purely high-impact pressure. Inside the void, several fragments are detected. According to EDS maps given in Figs. 4(g−i), these fragments share the same chemical compositions with other materials in the melted zone, indicating their formation being a result of material spalling of the mixture due to the existence of void. In summary, all of these observations reveal complex interface morphologies, suggesting that the interface materials undergo perplexing plastic deformations and reactions which will be further discussed in the following sections.

3.2 Wave evolution

To elucidate the complex interfacial phenomena, the wave evolution was carefully studied by SPH simulation, with the key results in Fig. 5. During the oblique collision, an intense interfacial shear instability arises from the variation of tangential velocity, which induces the interfacial materials to initiate a circular movement, and leads

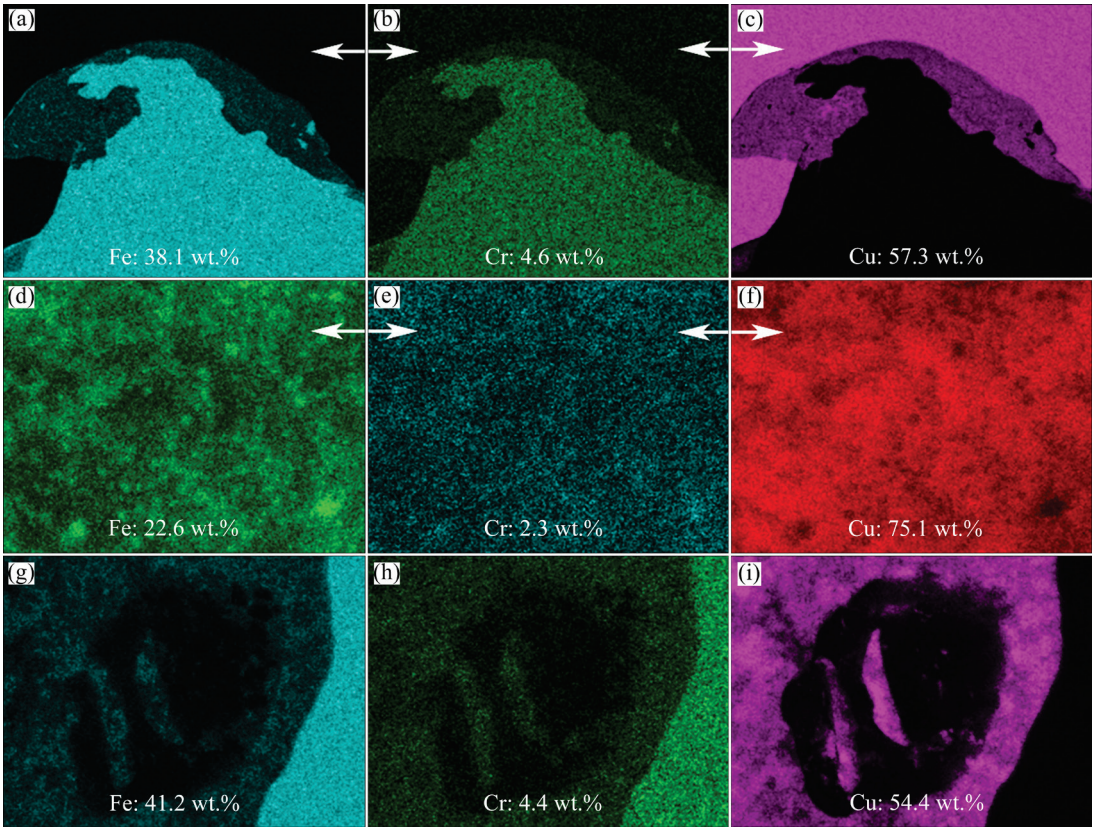

Fig. 4 EDS map scanning results within three selected zones labeled in Fig. 3: (a−c) EDS1 in Fig. 3(a); (d−f) EDS2 in Fig. 3(c); (g−i) EDS3 in Fig. 3(e)

to the formation of a protrusion on base plate, as shown in Figs. 5(a) and (a_1). The protrusion grows quickly upward and the flyer plate continues to move downward, leading to an oblique collision in a speed level of 2 km/s. At this moment, a geometric cavity is noticeable on the left of the protrusion, as labeled in Fig. 5(b). Then, the cavity is filled with downward particles from flyer plate, which will further produce an impact on the left side of the protrusion, as displayed in Fig. 5(b_1). As a result, an inward arc-shaped profile is formed at the left boundary of the protrusion, as labeled in Fig. 5(c). Moreover, at this stage, the motion state of particles on the top of the protrusion is disturbed by the downward particles of flyer plate, leading to part of particles moving towards the left of the protrusion. As the left movement goes on, some Fe fragments are observed as islands in Cu matrix (Fig. 5(d)), due to the strong mutual penetration of the two materials. Meanwhile, the converging particles are further mixed by a strong stirring movement, indicated by the circular arrows of velocity vector in Fig. 5(d_1). As the evolution progresses, the protrusion grows further and a left branch is formed, as shown in Fig. 5(e). At this stage, the circular movement is broken by continuous compaction from flyer plate, and the velocities of different particles tend to be the same, indicating that the wave evolution is complete. After reviewing the whole process of wave development, it can be clearly seen that the interface materials undergo an extremely large plastic deformation, which will produce a significant amount of heat near the interface. Figures 5(a_1−e_1) also give an opportunity to investigate the melting phenomena at the interface (marked by red color), where, in terms of occurrence location and shape, the predicted high-temperature regions in Fig. 5(f) show good agreements with the SEM observations displayed in Fig. 5(f_1).

3.3 Grain structure

According to crystallographic theory [38], the grain structure evolution depends on material properties and thermodynamic conditions like pressure, temperature and deformation. Since the EW interface shows a high degree heterogeneity as

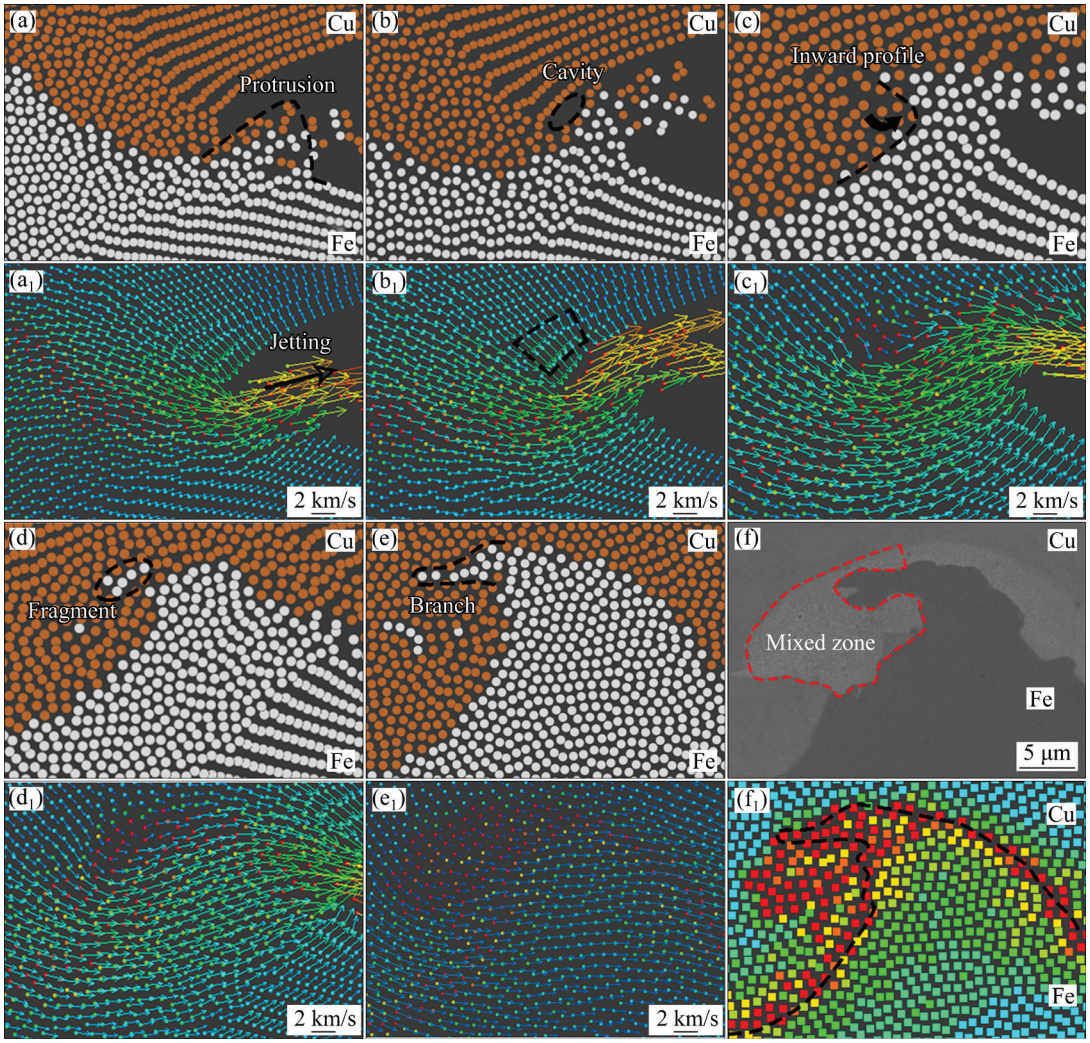

Fig. 5 Sequential development of wave obtained by SPH simulation: (a−e) Material distribution; (a_1−e_1) Velocity vector collaborated with temperature distribution maps; (f) SEM image showing crest; (f_1) Temperature distribution corresponding to (f)

revealed in Section 3.1, it is foreseeable that there is a complex grain structure distribution in space. To fully reveal these grain structure characteristics, four typical areas respectively representing Cu matrix, Fe matrix, direct bonding interface, and vortex area were subjected to the EBSD analysis, and the corresponding results are presented and compared in the following sections.

3.3.1 Matrixes of Cu and Fe

Figure 6(a) shows the inverse pole figure (IPF) of Cu matrix, revealing rectangle-like grains with a mean diameter of ~4 μm (Fig. 6(b)) and mean grain shape factor (R) of ~3.8, where R is the ratio of the length to the width of the approximately elliptic grain, indicating the grain elongated degree [39]. Figure 6(a) also reveals the typical twins characterized by parallel line through the grains. Especially, these twins can be divided into two types, namely complete twins throughout the whole grains and incomplete twins that do not penetrate through the grains. The formation of the twin is due to annealing process of the initial materials, which leads to the migration of the grain boundary and atoms in the growing grains accidentally staggering along the {111} plane [40]. Figure 6(c) shows the recrystallization distribution diagram, in which the recrystallized grains are marked by yellow, while the blue and red represent substructured and deformed grains, respectively. Clearly, the majority of Cu grains are substructured grains, while some deformed grains gather together near the interface. The width of the deformed layer is approximately 40 μm, which is a consequence of strong plastic deformation favored by the EW process.

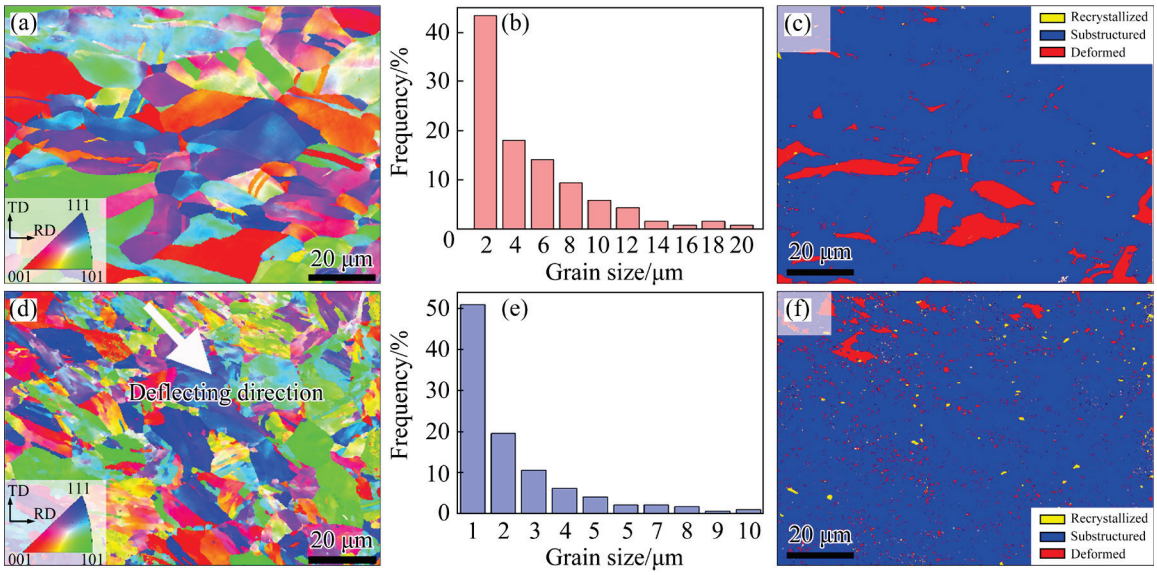

Fig. 6 EBSD IPF orientation maps of Cu (a) and Fe (d), grain size distributions of Cu (b) and Fe (e), and recrystallization distribution diagrams of Cu (c) and Fe (f)

The global grain information of Fe matrix is provided in Figs. 6(d−f) using the same figure types with the Cu matrix. Figure 6(d) shows the IPF coloring, revealing typical martensite microstructures consisted of banding grains with mean grain size of ~2 μm and mean grain shape factor R of ~2.3. According to Figs. 6(d) and (e), a large number of fine grains (~1 μm) are concentrated in the region adjacent to the interface, while in the area far away from the interface, the grains are dominated by a higher average diameter of ~5 μm. The variation in grain size is caused by plastic deformation during the EW process. As illustrated in Fig. 6(f), a severe deformed layer labeled by red color is well visible in the area near the interface. The width of the deformed layer is approximately 20 μm, which is slightly lower than that of Cu matrix. In particular, these deformed grains show a nearly uniform elongated direction, as labeled by white arrow in Fig. 6(d). This characteristic is due to the transmission of stress waves from collision, where the crystal structures deformed and deflected along the stress direction (the stress direction in the Fe matrix is approximately the same).

Figure 7 shows the pole figures (PFs) of Cu and Fe matrixes, which are the statistical results of the grains in Fig. 6. For Cu matrix, a strong texture of {001}⟨010⟩ with a cumulative density of 6.03 is identified, while the Fe matrix possesses a relatively weak texture of {122}⟨310⟩, with a density of 3.98. The different cumulative densities between Cu and Fe matrixes are induced by different levels of plastic deformation, as shown in Fig. 6. It is well known that shear deformation is a nearly ideal process for texture formation [41]. During EW process, the high-speed oblique impact produces strong shearing stresses, resulting in that some crystals near the interface deflect uniformly and thus exhibit a preferred orientation.

3.3.2 Direct bonding interface

The direct bonding interface without a transition layer is an ideal bonding mode in EW, due to the absence of microscopic defects [42]. The EBSD results conducted on this type of zone are illustrated in Figs. 8−10. Figure 8(a) shows the IPF map, revealing remarkable changes of metallurgical structure near the interface. In Cu matrix, the grains are significantly elongated, with length up to 10−100 μm and width of only 1−2 μm. These elongated grains are severely bent along the wave interface, well confirming the material movement predicted by SPH simulation in Section 3.2. It should be noted that the colors are inconsistent within grain boundaries for many grains, for instance, the grain in blue color contains green micro regions. This observation indicates orientation changes within the grain and reflects the large deformation in the micro regions. In particular, there are several deformation twins or shear bands which arrange in nearly periodic, as marked by

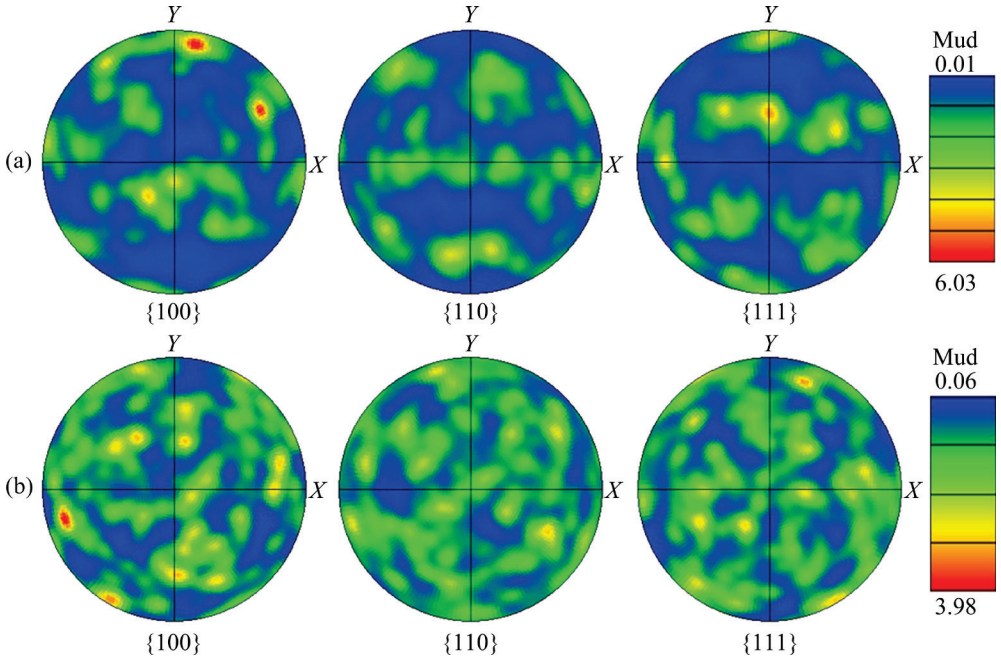

Fig. 7 Pole figures of Cu (a) and Fe (b) near bonding interface

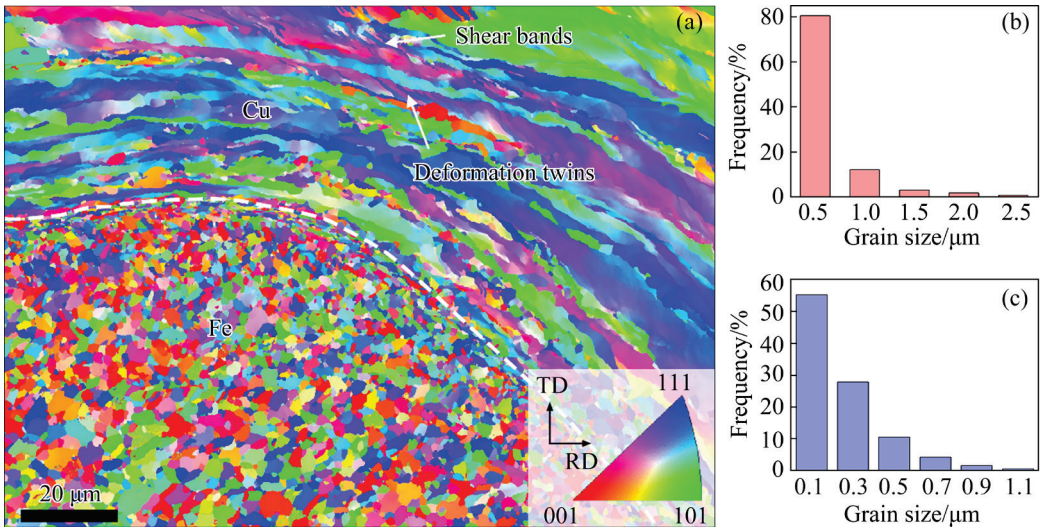

Fig. 8 EBSD IPF orientation map of Cu/Fe direct bonding interface (a), and grain size distributions of Cu (b) and Fe (c)

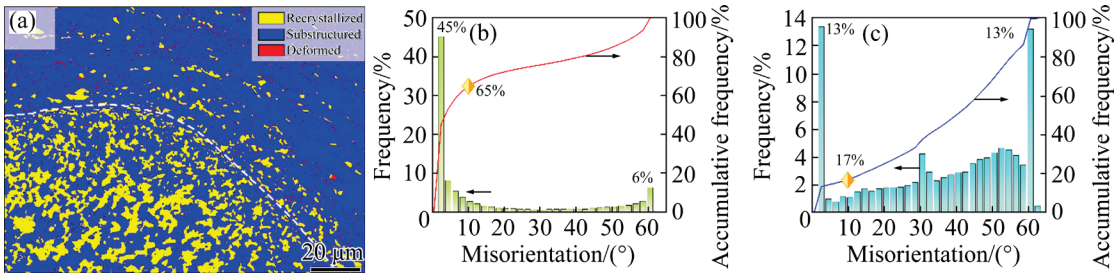

Fig. 9 Recrystallization distribution diagram of Cu/Fe direct bonding interface (a), and misorientation angle distributions of Cu (b) and Fe (c)

arrows in Fig. 8(a). According to the previous studies [43], the deformation twins corresponded to the peak of 60° in the distribution histograms of the grain boundary misorientation in Fig. 9(b). Besides the elongated grains, there are also some fine equiaxed grains with a size level of 100 nm, which

preferentially locate at the grain boundary and occasionally exist within the large grains. It can be inferred from this characteristic that the dynamic recrystallization occurs in local regions. Unlike the Cu matrix, the grains in Fe matrix are characterized by fine equiaxed structures, without any large elongated grain. Combined with the equivalent diameter distribution in Fig. 8(c), it can be found that the grain size varies widely in this zone, where the equivalent diameter is about 100 nm in the neighborhood of the interface, and gradually increases to ~800 nm with increasing distance from the interface. Apparently, the average grain size level in this zone is far lower than the original one, as revealed in Fig. 6(d). This grain variation feature is of particular interest, which will be discussed in following section. These equiaxed grains in Fe matrix also exhibit regular smooth grain boundaries, without dislocations, cell-type arrays, and deformation bands typically observed in highly deformed metals, which suggests that strong recovery and even recrystallization may occur in this zone during the welding process.

Figure 9(a) shows recrystallization distribution diagram of the direct bonding interface. In Cu matrix, blue color occupies the major proportion and only small areas show yellow, indicating that recrystallization only occurs in local small region. In Fe matrix, however, yellow becomes the dominant color, representing that the vast majority of the grains have finished recrystallization process. The recrystallization distribution diagram is full consistent with the above analysis. Figures 9(b) and (c) give the distributions of misorientation angle for Cu and Fe matrices, respectively. In Cu matrix, the fraction of low angle grain boundaries (LAGBs, ≤10°) is as high as 65%, while that is found to be only 17% in Fe matrix. The formation of high dense LAGBs is due to the movement and rearrangement of the dislocation, induced by strong plastic deformation [26,44]. In contrast, the lower fraction of LAGBs in Fe matrix is a consequence of dynamic recovery and recrystallization. In this condition, the grain boundary migration occurs as a result of being driven by stored strain and heat energy, which leads to the LAGBs being changed to high angle grain boundaries (HAGBs). Figure 10 shows the PFs of Cu and Fe matrixes, which reveals a strong texture of {212}⟨231⟩ for Cu matrix, but no obvious texture is found in Fe matrix. This is because the recrystallized grains grow in random directions, which erases the initial texture in Fe matrix.

3.3.3 Vortex area

The grain structures in vortex area, important to assess the key properties of the EW interface, are provided in Figs. 11−13. As shown in Fig. 11, the most striking feature in the vortex area is the ultra-fine grains with a mean size of 300 nm, which

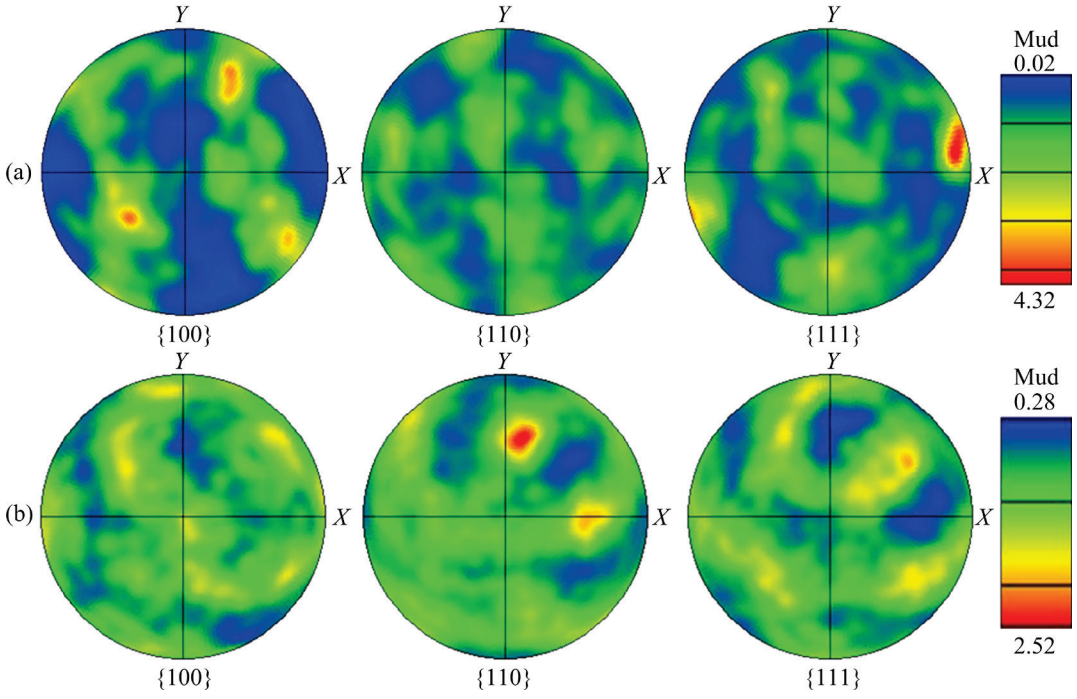

Fig. 10 Pole figures of Cu (a) and Fe (b) at direct bonding interface

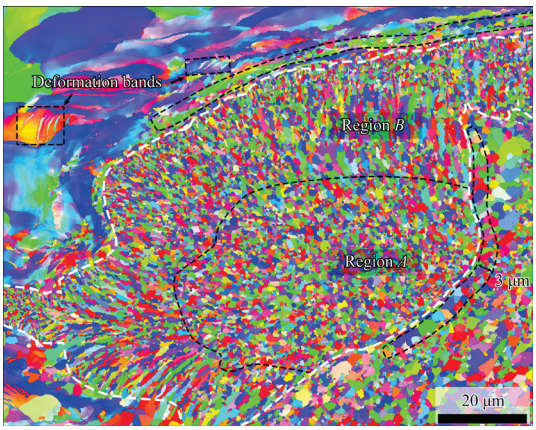

Fig. 11 IPF orientation map of Cu/Fe vortex area

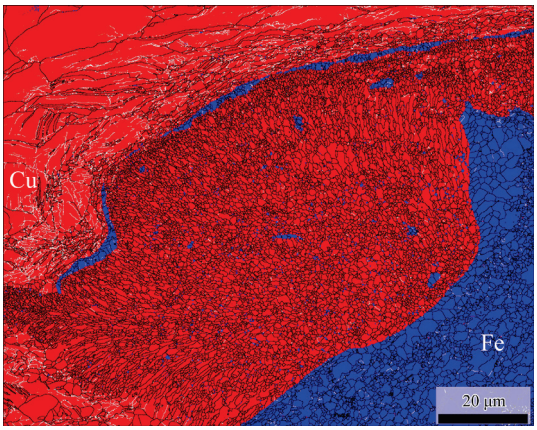

Fig. 12 Phase and grain boundary distributions of Cu/Fe vortex area

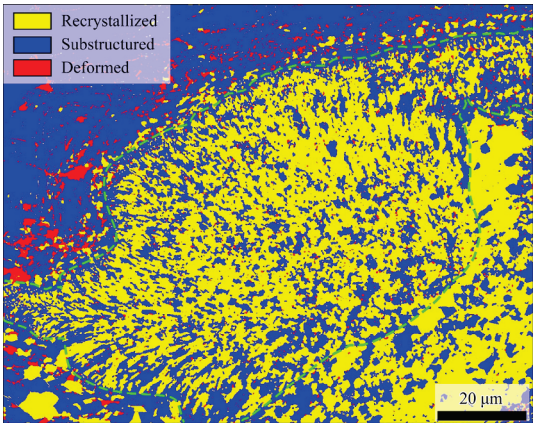

Fig. 13 Recrystallization distribution diagram of Cu/Fe vortex area

is far lower than that of the Cu and Fe matrixes. Although the average size level is low, these grains show a heterogeneous spatial distribution with dispersed shapes and varying diameters. For region near the Fe matrix (Region *A* in Fig. 11), the grains are characterized by equiaxed structures. Further, these equiaxed grains can be roughly classified by size into two classes, namely, the relatively coarse grains with a diameter of ~500 nm and ultra-fine nanoscale grains of only ~50 nm. The coarse grains occupy the major proportion in this zone, while the ultra-fine nanoscale grains are relatively rare, which are mainly located at grain boundaries of the large grains. Overall speaking, this region shows a uniform grain distribution in space. Unlike Region *A*, only a small number of equiaxed grains are found in region near the Cu matrix (Region *B* in Fig. 11). Instead, this region is dominated by columnar grains that grow perpendicularly to interfaces between Cu matrix and vortex zone. These columnar structures are the evidence of melting process, as they are similar to the microstructures of casting [29,36]. In addition, the sizes of these columnar grains change with the spatial position. The grains near the interface are smaller, with a width of ~100 nm and a length of ~1 μm, while those far away from the interface are characterized by larger size, with a width of ~200 nm and a length of ~4 μm. It can be also found from Fig. 11 that the existence of vortex area significantly affects the grain structures of the surrounding parent materials. In Fe matrix, there is an apparent vortex-affected layer along with the interface, which is characterized by a larger grain size than the area far away from the interface, as labeled by black dotted line in Fig. 11. The width of the vortex-affected layer is about 3 μm, in which the grains exhibit relatively uniform size distribution without the ultrafine nanoscale grains, indicating that the grains in this area experienced a higher degree growth. In Cu matrix, on the contrary, an apparent fine grain layer is found along the interface, as highlighted by the black dash line. In the fine grain layer, both equiaxed and elongated grains can be found, which are far smaller than the grains far away from the interface. Also, a highly deformed region that contains lots of twins and deformation bands is observed in the area slightly away from the interface, which is similar to the results observed at the direct bonding interface.

Figure 12 shows the phase distributions, where the red and blue represent Cu and Fe, respectively. It can be found that the Cu is the dominant phase in vortex area, which is consistent with previous EDS result. The Fe phase is mainly distributed at grain

boundaries of Cu/Fe in the form of discrete points, and only a small number of Fe phases are aggregated into micro volumes. Especially, we can find that the grains with Fe phase show a lower size level, and the similar phenomenon can also be found in previous work [40]. This result is related to pinning effect in grain growth process, where the Fe phase firstly solidifies into small particles due to the higher melting point, which are randomly distributed in Cu solution, and play an inhibiting role in the subsequent growth of Cu grains. Figure 12 also shows grain boundary situation, in which the black lines represent HAGBs, while the white lines correspond to LAGBs. Clearly, the grains in Fe matrix and vortex area mainly have the HAGBs, while the Cu matrix is dominated by LAGBs. This fact reflects different grain formation mechanisms, where the Fe matrix and vortex area undergo a process of recrystallization, and the grains in Cu matrix are a result of severe deformation, as indicated in Fig. 13.

3.4 Nano-indentation hardness

To correlate the grain changes with the mechanical properties, nanoindentation tests focusing on the interface region were performed, with the key results given in Fig. 14. As shown in Fig. 14(a), three types of areas respectively representing Cu matrix, Fe matrix, and mixture (vortex zone) were subjected to nano-indentation analyses. It is clear from Fig. 14(a) that the hardness values of the same material are at the same level. Especially, the hardness of the mixture in vortex area is consistent with that in the common transition region at the interface. This fact indicates that the melted zones at different locations share the similar material composition and grain structure, suggesting that they have the same formation mechanism. Figure 14(b) shows the typical load−depth curves of the three materials, where, under the same loading conditions, the indentation depths of Cu, Fe and mixture are found to be 440, 513 and 676 nm, respectively. Figure 14(c) compares the average nano-hardness values of the three materials, in which the Cu matrix possesses the smallest nano-hardness of 2.1 GPa, while Fe matrix exhibits the highest value of 4.8 GPa. The average hardness value of the mixture is determined to be 3.6 GPa, which is close to the arithmetic average of the hardness of Cu and Fe matrixes. This is slightly unexpected since the Cu is the main element of the melting area (accounting for 75%, as

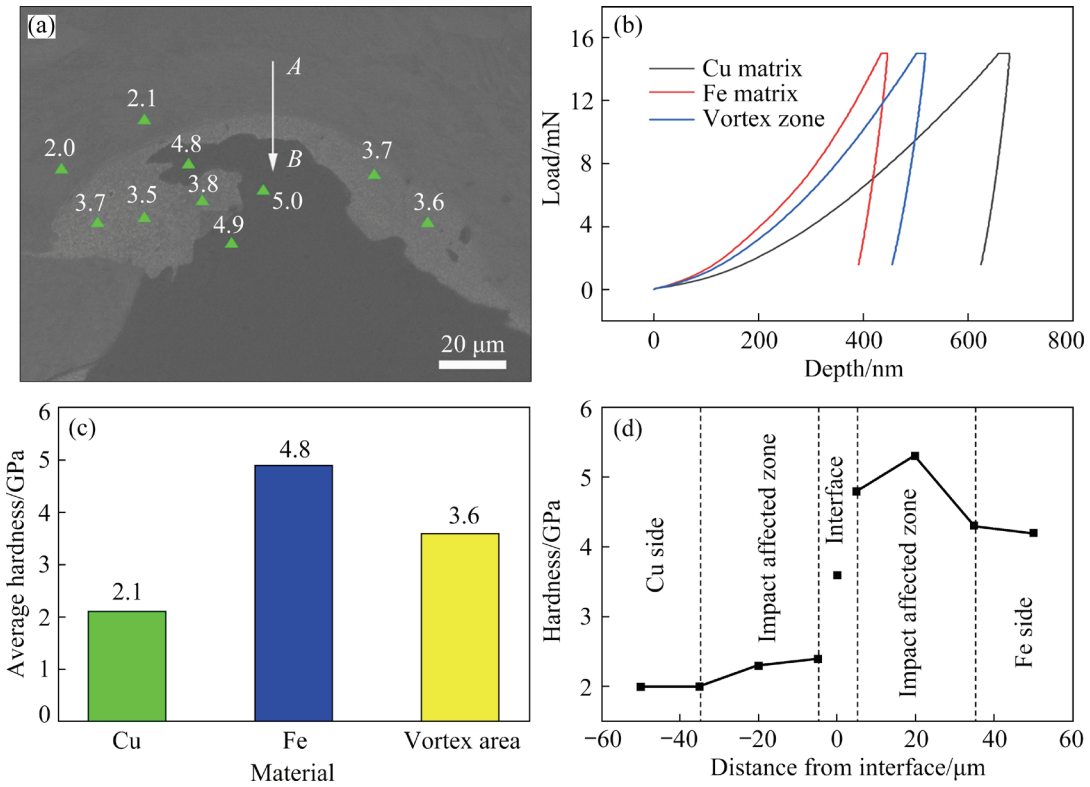

Fig. 14 SEM image showing test positions and corresponding hardness values (GPa) (a), typical load−depth curves for different materials (b), mean hardness values of different materials (c), and hardness profile across interface (d)

revealed by EDS analysis), and there is no intermetallic compound between the Cu and Fe elements. One of possible explanations is that the ultra-fine grain structures as shown in Fig. 11 effectively increase the hardness of the mixture. Figure 14(d) gives hardness profile across the bonding interface, with the test positions marked by *AB* in Fig. 14(a). As shown in Fig. 14(d), the materials near to the interface exhibit higher levels of hardness than those far away from the interface, and the widths of the high hardness zones are about 40 μm. This result is consistent with the work of BINA et al [45]. Referring to the EBSD results, the increase in hardness near the interface can be considered as a consequence of grain structure changes. On Cu side, there are impact-induced characteristics like dislocations, cellular structures, shear bands, and deformation twins, while on Fe side, the grains are replaced by finer equiaxed structures due to dynamic recrystallization. These grain changes enable to increase grain boundary area, and thus increase the resistance of the material to the external loadings [46]. It should be noted that the regions at the interface present lower hardness compared to the other region in the impact affected zone for Fe matrix. This may be because Fe matrix near interface is surrounded by the melted zone, as displayed in Fig. 14(a). In this condition, the grains undergo a further growth process due to the heat transfer, as shown in Fig. 11(a).

4 Discussion

4.1 Evolution model of wavy interface

The wavy evolution at the EW interface has been earlier addressed by ABRAHAMSON [14], who proposed a phenomenological model to understand the formation of the peculiar structure. Then, this model was further developed by BAHRANI et al [15] and BATAEV et al [23], and became the most widely accepted mechanism in the EW field. Figure 15 shows the feature-by-feature comparison of Bahrani−Black−Crossland model [15] and simulation-based evolution diagram. Clearly, the simulation-based model confirms several important insights about the wave evolution in the

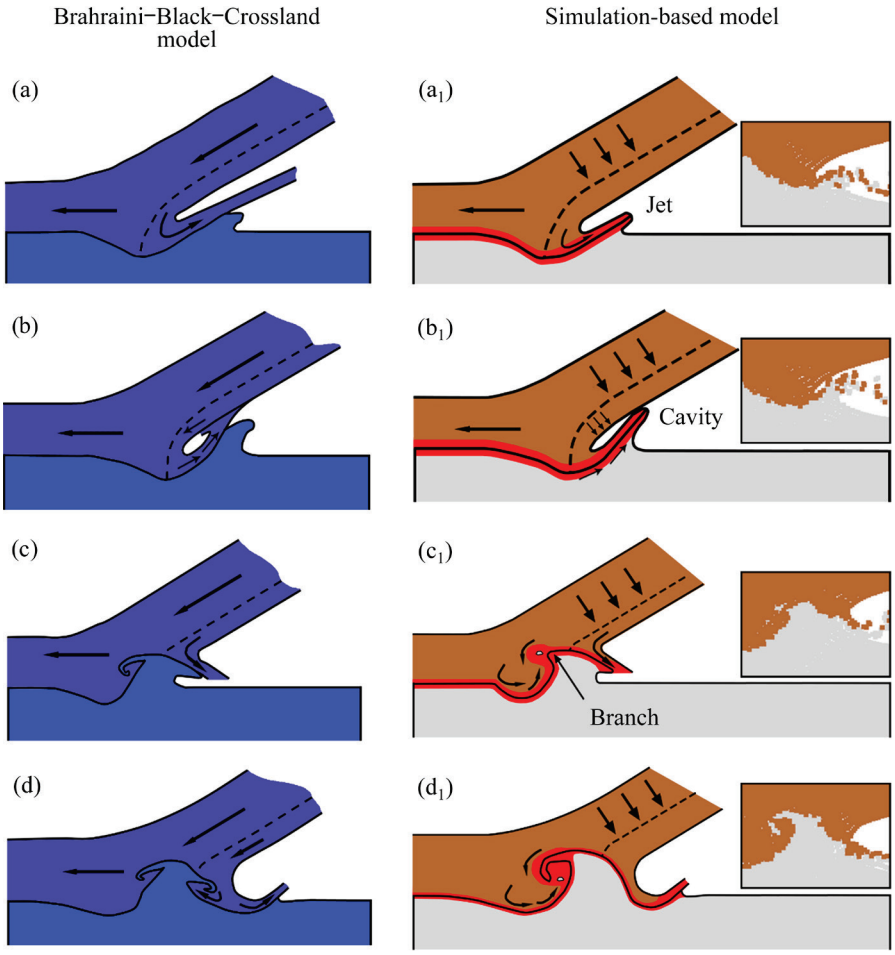

Fig. 15 Comparison of Bahrani−Black−Crossland model (a−d) and simulation-based model (a_1−d_1) evolution diagrams

classical theories. Firstly, in the simulation data, jets consisting of both the surface layers of the colliding plate are observed in front of the collision point, which well verifies the the self-cleaning assumption [47], namely jets wipe off the dirty of the raw materials and establish a clean contact for the upcoming metallurgical bonding. Secondly, the simulation model reveals that the essential mechanism of wave formation is the successive interaction between the jetting and the colliding plates, which shows good agreements with the Bahrani−Black−Crossland model and previous simulation results [15,23,27,48]. Lastly, during the initial collision stage (Figs. 15(b) and (b_1)), the two models simultaneously reveal the formation of geometric cavity on the left of the hump. Gradually, the cavity is filled with surrounding materials, and a specific vortex structure with distinctive rotation characteristics is formed in this zone, as shown in Figs. 15(c) and (c_1).

The model developed in this work also shows some differences and provides more details when compared to the classical model and previous simulation data. Firstly, in the Bahrani−Black−Crossland model, the left boundary of the wave is characterized by straight line, as shown in Fig. 15(d); while the observations in Fig. 3(c) show an inward arc-shaped profile on the left side of the wave. In fact, the formation of such an arc-shaped wave boundary is a common phenomenon that has been observed in many welding systems, referring to, e.g., Ti/Fe [27,49], W/Cu [50], and Ti/Cu [11,51]. The simulation-based model provides an excellent description on evolution process of the arc-shaped wave boundary and gives an opportunity to explore the associated mechanism. As shown in Fig. 15(a_1), it is clear that the formation of a protrusion on the base plate is governed by shear instability, which induces a remarkable circular movement and leads to the newly formed protrusion presenting a slight arc-shaped profile. Moreover, due to the existence of the geometric cavity, the middle part of the arc-shaped protrusion is further subjected to an impact from the flyer plate, as shown in Fig. 15(b_1). The above two behaviors result in the inward arc-shaped profile for the left boundary of the protrusion, as shown in Fig. 15(c_1). Secondly, one may also notice that the branch on the left side of the wave is formed gradually after it leaves the collision point. As shown in Fig. 15(b_1), the flyer plate moves diagonally downward, which depresses and elongates the protrusion on base plate, and accordingly, a small branch (marked in Fig. 15(c_1)) is formed on the left side of the protrusion. Then, the small branch gradually grows thicker and longer, driven by the early formed circular motion. It should be noted that the evolution of branch is accompanied by intense interpenetration between the two materials, which leads to the participating materials being broken and the formation of fragmentations, as marked by white color zones in Figs. 15(c_1) and (d_1). This finding makes it possible to explain why sometimes the islands of Fe are enclosed within the melted zones, as displayed in Fig. 3(e). Thirdly, the simulation-based model gives an opportunity to investigate the melting phenomena at the interface (marked by red color in Figs. 15(a_1−d_1), where an almost uniform layer of the melt is formed near the collision point, and then the melt moves along the wave interface and gradually converges to the left side of the wave, and accordingly the layer of the melt at the interface becomes thinner. This process indicates that the melted zones at different locations share the same formation mechanism, and explains the reasons why different melted zones have the similar mechanical properties. Finally, the simulation-based model provides a reasonable explanation for the formation of circular cavities observed experimentally, where the trapped empty space followed by intense stirring motion enables to establish a favorable condition for the pore nucleation.

4.2 Grain distribution characteristics and associated mechanisms

As revealed in Section 3.1, the EW process induces a dramatic microstructure evolution and leads to the formation of diverse metallurgical structures in the neighborhood of the interface. To get a comprehensive understanding on the diverse grain structures and explore the associated mechanisms, Fig. 16 shows the schematic diagram of grain distribution together with thermodynamic state predicted by SPH simulation. It is evident from Fig. 16(a) that the grains in different regions present different features. Clearly, vortex region is composed of two types of ultrafine grains, namely, columnar structures near the Cu matrix and equiaxed structures near the Fe matrix. According

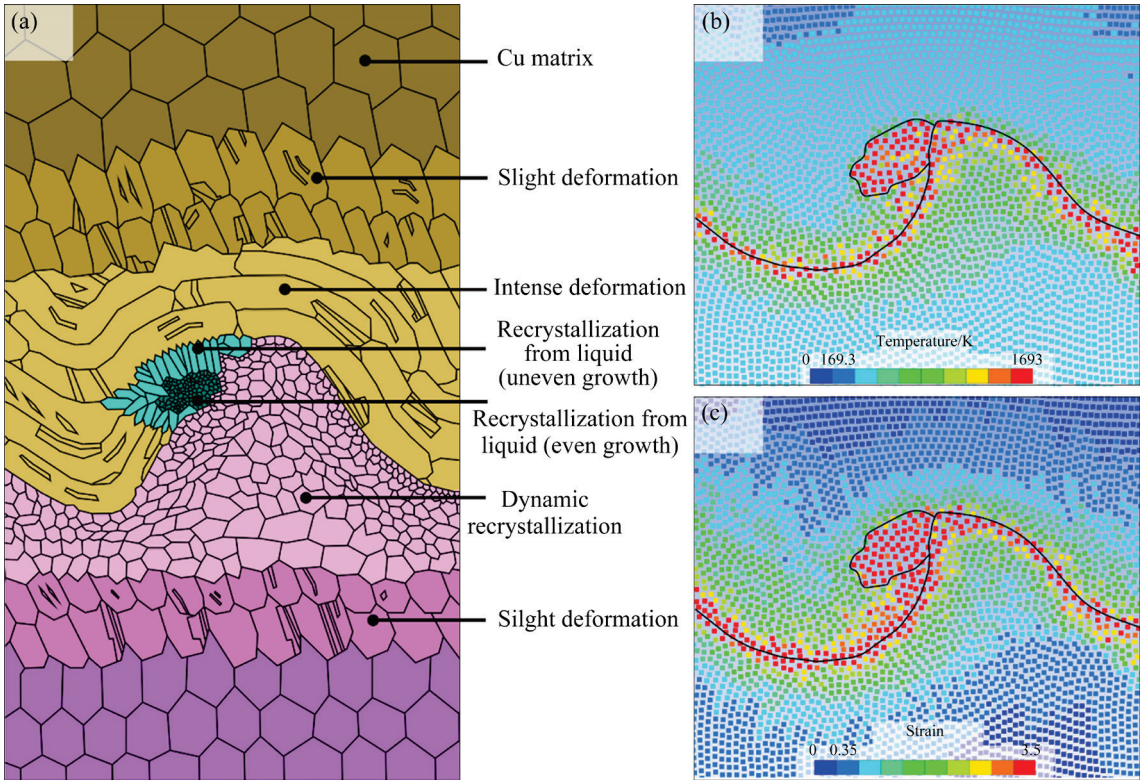

Fig. 16 Schematic diagrams of grain distribution (a), temperature distribution using enlarged view (b), and plastic strain distribution using enlarged view (c)

to simulation results in Figs. 16(b) and (c), the two types of ultrafine grains share the same formation mechanism, where the grains within the vortex region nucleate directly from the liquid induced by ultra-high temperature followed by rapid cooling process. Different grain shapes are related to various growth directions. As shown in Fig. 16(b), the ultrahigh temperature gradient at the interface between vortex region and Cu matrix forces the surrounding grains to grow along the highest gradient direction, while there is no obvious temperature gradient at the interface between vortex region and Fe matrix, and accordingly, the neighboring grains grow in a random direction. Moving to the region close to the Cu/Fe interface, elongated curved grains related to deformation process are found on Cu side, while equiaxed fine grains generated by dynamic recovery and recrystallization are formed on Fe side. The diverse grain features on the two sides of interface can be well explained by the predicted thermodynamic parameters. As shown in Fig. 16(c), it is clear that the materials on both sides of the interface undergo dramatic deformation processes, identified by the high plastic strain of ~2. Generally, the grain nucleation and growth in deformation zone need the temperature exceeding ~0.5T_m (T_m is the melting point) [52]. Thus, the recrystallization temperatures of the Cu and Fe matrixes are estimated to be ~700 K (T_m=1350 K) and ~900 K (T_m=1795 K), respectively. Based on this, it is clear from Fig. 16(b) that the temperature (~500 K) in Cu matrix is lower than its recrystallization temperature, while the temperature (1100 K) in Fe matrix is high enough to trigger the recrystallization process. It should be noted that the grain size in Fe matrix gradually increases with increasing distance from interface, as shown in Fig. 16(a). This result is slightly unexpected as CHU et al [27] observed the opposite trend systems in Ti/Fe welding systems, where the grain adjacent to the interface underwent a growth process due to the higher temperature. One of possible explanations is that the high thermal conductivity of Cu leads to rapid cooling for the surrounding Fe matrix, which inhibits further grain growth process. With increasing distance from interface, slightly deformed layers characterized by uniform elongated structure and local refinement are observed on both sides of the interface, indicating that the two regions are less affected by

the impact process. This result gets the powerful support of simulated data, where the extreme thermodynamic states are always tightly confined to the interfaces, as displayed in Figs. 16(b) and (c). This fact well confirms the ability of EW technique to minimize welding affected zone and save the original properties of the parent metals.

5 Conclusions

(1) The individual wave is characterized by asymmetrical geometry, where the left side of the wave presents an inward arc-shaped profile with a well defined branch at the top, while the right boundary is a slight outward curve. The special geometric features on the left side can be attributed to the combined action of circular movement caused by shear instability and the impact of the flyer plate to the middle part of the wave due to the cavity formed early.

(2) The formation of large melt pocket in the vortex zone is due to the convergent motion of the melting materials, driven by extrusion and shear instability. The intense circular motion together with the trapped empty space is responsible for circular void observed in the center of melted zone.

(3) The multi-scale EBSD analyses reveal that the vortex zone is built by columnar grains near the Cu matrix and fine equiaxed grains near the Fe matrix. Near the interface, the Cu grains are elongated and severely curved, with abundant randomly distributed dislocations, shear bands and deformation twins, while the Fe grains are featured by dislocation-free equiaxed structures with a well-defined increasing tendency of grain size with increasing distance from the interface.

(4) The evolution mechanism of the grains in vortex zone can be explained by the following sequential process: melting, mechanical mixing, Fe grain nucleation, Cu grain nucleation, and growth, where the earlier solidified Fe phase will play an inhibiting role in the subsequent growth of Cu grains, and various temperature gradients are responsible for different grain shapes.

(5) Correlations between the grain structures and mechanical properties are well established by nanoindentation tests, where the as-deformed grains show the highest hardness value, while the hardness of the dislocation-free recrystallized grains is relatively low, but still higher than the original value.

CRediT authorship contribution statement

Ming YANG: Perform the experiment and write the manuscript; **Bing-yuan ZHANG:** Perform the numerical simulation and data analysis; **Hong-hao MA:** Provide experimental conditions and financial support; **Jin-xiang WANG:** Polish the language; **Jia-yi XIONG:** Revise the paper.

Declaration of competing interest

The authors declare that they have no known competing financial interests or personal relationships that could have appeared to influence the work reported in this paper.

Data availability

The raw/processed data required to reproduce these findings cannot be shared at this time due to technical or time limitations.

Acknowledgments

This research was supported by the National Science Foundation for Young Scientists of China (Nos. 12102427, 12102202), and the Chinese Innovation and Entrepreneurship Training Program for College Students (No. 202210288112X).

References

[1] SUNNY S, GLEASON G, MATHEWS R, MALIK A. Simulation of laser impact welding for dissimilar additively manufactured foils considering influence of inhomogeneous microstructure [J]. Materials & Design, 2021, 198: 109372.

[2] LI Z, BESLIN, E, DEN BAKKER A J, SCAMANS G, DANAIE M, WILLIAMS C A, ASSADI H. Bonding and microstructure evolution in electromagnetic pulse welding of hardenable Al alloys [J]. Journal of Materials Processing Technology, 2021, 290: 116965.

[3] YANG Ming, MA Hong-hao, YAO Da-mao, SHEN Zhao-wu. Experimental study for manufacturing 316L/CuCrZr hollow structural component [J]. Fusion Engineering and Design, 2019, 144: 107–118.

[4] FINDIK F. Recent developments in explosive welding [J]. Materials & Design, 2011, 32: 1081−1093.

[5] LYSAK V I, KUZMIN S V. Energy balance during explosive welding [J]. Journal of Materials Processing Technology, 2015, 222: 356−364.

[6] YANG Ming, XU Jun-feng, MA Hong-hao, SHEN Zhao-wu, ZHANG Bing-yuan, CHEN Dai-guo. Elucidating the formation mechanism of the vortex at the Ta/Fe explosively welded interface using microstructure characterizations and numerical simulations [J]. Metallurgical and Materials Transactions A, 2022, 53: 364−369.

[7] GLEASON G, SUNNY S, MATHEWS R, MALIK A. Numerical investigation of the transient interfacial material behavior during laser impact welding [J]. Scripta Materialia, 2022, 208: 114325.

[8] GREENBERG B A, IVANOV M A, RYBIN V V, ELKINA O A, ANTONOVA O V, PATSELOV A M, INOZEMTSEV A V, PLOTNIKOV A V, VOLKOVA A Y, BESSHAPOSHNIKOV Y P. The problem of intermixing of metals possessing no mutual solubility upon explosion welding (Cu−Ta, Fe−Ag, Al−Ta) [J]. Materials Characterization, 2013, 75: 51−62.

[9] LEE T, NASSIRI A, DITTRICH T, VIVEK A, DAEHN G. Microstructure development in impact welding of a model system [J]. Scripta Materialia, 2020, 178: 203−206.

[10] PAUL H, MISZCZYK M M, CHULIST R, PRAZMOWSKI M, MORGIEL J, GALKA A, FARYNA M, BRISSET F. Microstructure and phase constitution in the bonding zone of explosively welded tantalum and stainless steel sheets [J]. Materials & Design, 2018, 153: 177−189.

[11] PAUL H, CHULIST R, MISZCZYK M, LITYNSKA-DOBRZYNSKA L, CIOS G, GALKA A, PETRZAK P, SZLEZYNGER M. Towards a better understanding of the phase transformations in explosively welded copper to titanium sheets [J]. Materials Science and Engineering: A, 2020, 784: 139285.

[12] WANG K F, SHANG S L, WANG Y X, VIVEK A, DAEHN G, LIU Z K, LI J J. Unveiling non-equilibrium metallurgical phases in dissimilar Al−Cu joints processed by vaporizing foil actuator welding [J]. Materials & Design, 2020, 186: 108306.

[13] LI J S, RAOELISON R N, SAPANATHAN T, HOU Y L, RACHIK M. Interface evolution during magnetic pulse welding under extremely high strain rate collision: mechanisms, thermomechanical kinetics and consequences [J]. Acta Materialia, 2020, 195: 404−415.

[14] ABRAHAMSON G R. Permanent periodic surface deformation due to a traveling jet [J]. Journal of Applied Mechanics, 1961, 28: 519−528.

[15] BAHRANI A S, BLACK T J, CROSSLAND B. The mechanics of wave formation in explosive welding [J]. Proceedings of the Royal Society of London Series A—Mathematical and Physical Sciences, 1967, 296: 123−136.

[16] BEN-ARTZY A, STERN A, FRAGE N, SHRIBMAN V, SADOT O. Wave formation mechanism in magnetic pulse welding [J]. International Journal of Impact Engineering, 2010, 37: 397−404.

[17] ROBINSON J L. Mechanics of wave formation in impact welding [J]. Philosophical Magazine, 1975, 31: 587−597.

[18] REID S R. A discussion of the mechanism of interface wave generation in explosive welding [J]. International Journal of Mechanical Sciences, 1974, 16: 399−413.

[19] EL-SOBKY H, BLAZYNSKI T Z. Experimental investigation of the mechanics of explosive welding by means of a liquid analogue [C]//Proceedings of the 5th International Conference on High Energy Rate Fabrication. Denver, Colorado, 1975: 1−21.

[20] ZHANG Z L, FENG D L, LIU M B. Investigation of explosive welding through whole process modeling using a density adaptive SPH method [J]. Journal of Manufacturing Processes, 2018, 35: 169−189.

[21] ZHANG Z L, LIU M B. Numerical studies on explosive welding with ANFO by using a density adaptive SPH method [J]. Journal of Manufacturing Processes, 2019, 41: 208−220.

[22] ZENG X Y, LI X Q, LI X J, MO F, YAN H H. Numerical study on the effect of thermal conduction on explosive welding interface [J]. The International Journal of Advanced Manufacturing Technology, 2019, 104: 2607−2617.

[23] BATAEV I A, TANAKA S, ZHOU Q, LAZURENKO D V, JUNIOR A J, BATAEV A A, HOKAMOTO K, MORI A, CHEN P. Towards better understanding of explosive welding by combination of numerical simulation and experimental study [J]. Materials & Design, 2019, 169: 107649.

[24] PAUL H, CHULIST R, LITYNSKA-DOBRZYNSKA L, PRAZMOWSKI M, FARYNA M, MANIA I, SZULC Z, MISZCZYK M M, KUREK A. Interfacial reactions and microstructure related properties of explosively welded tantalum and steel sheets with copper interlayer [J]. Materials & Design, 2021, 208: 109873.

[25] YANG M, MA H H, SHEN Z W, HUANG Z C, TIAN Q C, TIAN J. Dissimilar material welding of tantalum foil and Q235 steel plate using improved explosive welding technique [J]. Materials & Design, 2020, 186: 108348.

[26] LIU K Y, CHEN P W, RAN C, ZHOU Q, FENG J R, FAN X K, ZHU L. Investigation on the interfacial microstructure and mechanical properties of the W−Cu joints fabricated by hot explosive welding [J]. Journal of Materials Processing Technology, 2022, 300: 117400.

[27] CHU Q L, ZHANG M, LI J H, YAN C. Experimental and numerical investigation of microstructure and mechanical behavior of titanium/steel interfaces prepared by explosive welding [J]. Materials Science and Engineering: A, 2017, 689: 323−331.

[28] PAUL H, PETRZAK P, CHULIST R, MAJ L, MANIA I, PRAZMOWSKI M. Effect of impact loading and heat treatment on microstructure and properties of multi-layered AZ31/AA1050 plates fabricated by single-shot explosive welding [J]. Materials & Design, 2022, 214: 110411.

[29] ZHANG H, JIAO K X, ZHANG J L, LIU J P. Comparisons of the microstructures and micro-mechanical properties of copper/steel explosive-bonded wave interfaces [J]. Materials Science and Engineering: A, 2019, 756: 430−441.

[30] BATAEV I A, LAZURENKO D V, TANAKA S, HOKAMOTO K, BATAEV A A, GUO Y, JORGE A M. High cooling rates and metastable phases at the interfaces of explosively welded materials [J]. Acta Materialia, 2017, 135: 277−289.

[31] PAUL H, MORGIEL J, BAUDIN T, BRISSET F, PRAZMOWSKI M, MISZCZYK M. Characterization of explosive weld joints by TEM and SEM/EBSD [J]. Archives of metallurgy and materials, 2014, 59: 1129−1136.

[32] YANG M, MA H H, SHEN Z W, CHEN D G, DENG Y X. Microstructure and mechanical properties of Al−Fe meshing bonding interfaces manufactured by explosive welding [J]. Transactions of Nonferrous Metals Society of China, 2019, 29: 680−691.

[33] MEYERS M A. Dynamic behavior of materials [M]. New York: John Wiley & Sons, 1994.

[34] NASSIRI A, ZHANG S, LEE T, ABKE T, VIVEK A, KINSEY B, DAEHN C. Numerical investigation of CP-Ti & Cu110 impact welding using smoothed particle hydrodynamics and arbitrary Lagrangian−Eulerian methods [J]. Journal of Manufacturing Processes, 2017, 28: 558−564.

[35] JI C, CHEN L, LONG Y, XU Q J. Dynamic behaviors of multi-layered steel targets with air gaps subjected to the impact of EFP simulants [J]. International Journal of

Protective Structures, 2015, 6: 65−80.
[36] YANG M, XU J F, CHEN D G, MA H H, SHEN Z W, ZHANG B Y, TIAN J. Understanding interface evolution during explosive welding of silver foil and Q235 substrate through experimental observation coupled with simulation [J]. Applied Surface Science, 2021, 566: 150703.
[37] LI J S, SAPANATHAN T, RAOELISON R N, HOU Y L, SIMAR A, RACHIK M. On the complete interface development of Al/Cu magnetic pulse welding via experimental characterizations and multiphysics numerical simulations [J]. Journal of Materials Processing Technology, 2021, 296: 117185.
[38] ZHANG T T, WANG W X, ZHANG W, WEI Y, CAO X Q, YAN Z F, ZHOU J. Microstructure evolution and mechanical properties of an AA6061/AZ31B alloy plate fabricated by explosive welding [J]. Journal of Alloys and Compounds, 2018, 735: 1759−1768.
[39] COUTINHO Y A, ROONEY S C K, PAYTON E J. Analysis of EBSD grain size measurements using microstructure simulations and a customizable pattern matching library for grain perimeter estimation [J]. Metallurgical and Materials Transactions A, 2017, 48: 2375−2395.
[40] ZHANG H, JIAO K X, ZHANG Z J, LIU J P. Microstructure and mechanical properties investigations of copper-steel composite fabricated by explosive welding [J]. Materials Science and Engineering: A, 2018, 731: 278−287.
[41] SEGAL V M. Materials processing by simple shear [J]. Materials Science and Engineering: A, 1995, 197: 157−164.
[42] YANG M, MA H H, SHEN Z W. Study on self-restrained explosive welding with high energy efficiency [J]. The International Journal of Advanced Manufacturing Technology, 2018, 99: 3123−3132.
[43] GLADKOVSKY S V, KUTENEVA S V, SERGEEV S N. Microstructure and mechanical properties of sandwich copper/steel composites produced by explosive welding [J]. Materials Characterization, 2019, 154: 294−303.
[44] FRONCZEK D M, CHULIST R, LITYNSKA-DOBRZYNSKA L, KAC S, SCHELL N, KANIA Z, SZULC Z, WOJEWODA-BUDKA J. Microstructure and kinetics of intermetallic phase growth of three-layered A1050/AZ31/A1050 clads prepared by explosive welding combined with subsequent annealing [J]. Materials & Design, 2017, 130: 120−130.
[45] BINA M H, DEHGHANI F, SALIMI M, Effect of heat treatment on bonding interface in explosive welded copper/stainless steel [J]. Materials & Design, 2013, 45: 504−509.
[46] XU L Y, ZHU J, JING H Y, ZHAO L, LV X Q, HAN Y D, Effects of deep cryogenic treatment on the residual stress and mechanical properties of electron-beam-welded Ti−6Al−4V joints [J]. Materials Science and Engineering: A, 2016, 673: 503−510.
[47] DERIBAS A. Physics of hardening and welding by explosion [M]. Novosibirsk: Nauka, 1972.
[48] YANG M, XU J F, MA H H, LEI M Z, NI X J, SHEN Z W. Microstructure development during explosive welding of metal foil: Morphologies, mechanical behaviors and mechanisms [J]. Composites Part B: Engineering, 2021, 212: 108685.
[49] ZHOU Q, LIU R, RAN C, FAN K S, XIE J, CHEN P W. Effect of microstructure on mechanical properties of titanium-steel explosive welding interface [J]. Materials Science and Engineering: A, 2022, 830: 142260.
[50] LEI M Z, YANG M, NI X J, MA H H, XU S L. Experiment and simulation investigations on W/Cu components prepared by strong confinement thermal explosive welding [J]. Nuclear Materials and Energy, 2021, 29: 101086.
[51] MAHMOOD Y, CHEN P W, BATAEV I A, GAO X. Experimental and numerical investigations of interface properties of Ti_6Al_4V/CP-Ti/Copper composite plate prepared by explosive welding [J]. Defence Technology, 2021, 17: 1592−1601.
[52] NASSIRI A, ABKE T, DAEHN G. Investigation of melting phenomena in solid-state welding processes [J]. Scripta Materialia, 2019, 168: 61−66.

铜/钢爆炸焊接复合界面的显微组织及晶粒结构演化机理

杨 明[1]，张冰原[2]，马宏昊[2,3]，王金相[1]，熊家艺[1]

1. 南京理工大学 瞬态物理全国重点实验室，南京 210094；
2. 中国科学技术大学 中国科学院材料力学行为和设计重点实验室，合肥 230026；
3. 中国科学技术大学 火灾科学国家重点实验室，合肥 230026

摘 要：采用光滑粒子仿真、先进表征和理论分析相结合的方法，对铜/钢复合材料爆炸焊接过程中的界面瞬态行为进行深入研究，并详细阐述其显微组织演化机制。根据仿真数据重构波形完整的演化过程，并揭示各种界面特征的形成机制。多尺度 EBSD 分析表明，界面附近区域呈多样性的晶粒结构，其演化机制主要受塑性流动、动态再结晶和凝固形核三个过程的控制。最后，通过纳米压痕实验建立晶粒结构与力学性能之间的关系。

关键词：爆炸焊接；铜/钢复合材料；成波机理；晶粒结构；纳米压痕

(Edited by Wei-ping CHEN)